

# Effect of Machining on Shear-Zone Microstructure in Ti-15V-3Cr-3Al-3Sn: Conventional and Ultrasonically Assisted Turning

Q. Shi, Y.Y. Tse, R. Muhammad, A. Roy, V.V. Silberschmidt, and R.L. Higginson

(Submitted February 6, 2016; in revised form June 1, 2016; published online July 21, 2016)

This work systematically studied morphology of nano- and microstructures in primary and secondary shear zones of machining chips produced with two different machining methods: conventional and ultrasonically assisted turning. Electron backscatter diffraction and transmission electron microscopy showed that chips had similar microstructures for both machining techniques. The nanostructure in secondary shear zones was less homogeneous than that in primary shear zones. In addition, a heavily deformed layer was formed in a subsurface of Ti-15V-3Cr-3Al-3Sn work-pieces, replicating the microstructure of secondary shear zones of the machining chips, and elongated nanocrystalline grains in this layer were aligned with a tangential direction of turning.

**Keywords** machining, microstructure, shear zone, titanium, UAT

## 1. Introduction

In the past decades, titanium alloys have gained extensive applications in the aerospace and biomaterial industries, primarily thanks to their excellent mechanical properties, corrosion resistance, and biocompatibility. Apart from Ti-6Al-4V, which is the most prominent  $\alpha + \beta$  titanium alloy in the market, metastable  $\beta$ -titanium alloys, for instance Ti-15V-3Cr-3Al-3Sn, attracted substantial attention of the aerospace industry thanks to their high tensile strength and better deformability compared to those of  $\alpha$  or  $\alpha + \beta$  alloys (Ref 1). However,  $\beta$ -titanium alloys are notoriously hard to machine because of their low thermal conductivity and high chemical reactivity with tool materials (Ref 2, 3). Therefore, an advanced technique, ultrasonically assisted turning (UAT), was employed to improve machinability of the Ti-15V-3Cr-3Al-3Sn alloy (Ref 4-8). During UAT, a high-frequency vibration is imposed on the cutting tool (Ref 9-12), offering a number of benefits to the machining process including lower cutting forces (Ref 13) and improved finish of machined surface (Ref 10).

Q. Shi, Department of Mechanical and Electrical Engineering, University of Shaoxing, Shaoxing 312000, Zhejiang Province, China and Department of Materials, Loughborough University, Loughborough, Leicestershire LE11 3TU, UK; Y.Y. Tse and R.L. Higginson, Department of Materials, Loughborough University, Loughborough, Leicestershire LE11 3TU, UK; R. Muhammad, Department of Mechanical Engineering, CECOS University of IT and Emerging Sciences, Peshawar, Khyber Pakhtunkhwa, Pakistan; and A. Roy and V.V. Silberschmidt, Wolfson School of Mechanical and Manufacturing Engineering, Loughborough University, Loughborough, Leicestershire LE11 3TU, UK. Contact e-mails: q.shi@lboro.ac.uk, Y.Tse@lboro.ac.uk, R.Muhammad@cecos.edu.pk, A.Roy3@lboro.ac.uk, v.silberschmidt@lboro.ac.uk, and R.L.Higginson@lboro.ac.uk.

A number of researchers focused on machinability of titanium alloys (Ref 14-16), morphology of titanium alloy machining chips (Ref 17-22), and numerical simulations of chip formation (Ref 23-27); however, a very few studied the microstructure of machining chips, especially the nanostructure generated during the machining process. A systematic study of machining chips will help in the understanding of deformation characteristics of the materials exposed to different machining techniques.

During a traditional machining process, a tool is forced into a surface of the machined work-piece separating a chip from the parent material due to shear deformation along a primary shear zone (Ref 28). Generation of this zone involves severe strains localized in a narrow region, which may cause shear failure. In addition to the primary shear zone, friction between the formed chip and the tool's rake face can result in a secondary shear zone (Ref 28, 29). The schematic of primary and secondary shear zone with respect to the cutting force is illustrated in Fig. 1(a). In order to examine the shear strain introduced in the primary shear zone, the chips are modeled as parallel plates (Fig. 1b). The strain level is derived using the shear strain triangle shown in Fig. 1(c) (Ref 28):

$$\gamma = \frac{AC}{BD} = \frac{AD + DC}{BD} = \frac{AD}{BD} + \frac{DC}{BD} = \cot \phi + \tan(\phi - \alpha), \quad (\text{Eq 1})$$

where  $\gamma$  represents the shear strain,  $\alpha$  represents the tool rake angle ( $14^\circ$  in this study) (Ref 9, 10), and  $\phi$  represents the shear plane angle, which is given by

$$\tan \phi = \frac{t_0 \cos \alpha}{1 - \frac{t_0}{t_c} \sin \alpha}, \quad (\text{Eq 2})$$

where  $t_0$  represents the depth of cut, and  $t_c$  represents the chip thickness after machining.

As a result of generation of highly localized strains, the microstructures at the shear zones are distinct from those of the parent material. This study aims to reveal the character of

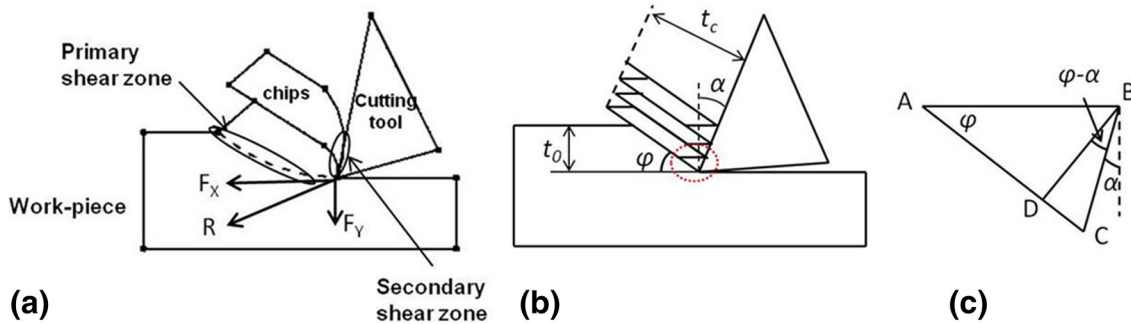


**Fig. 1** (a) Schematic of formation of primary and secondary shear zone:  $R$  is the resultant force,  $F_x$  is the main cutting force, and  $F_y$  is the feed force (after Ref 13), (b) the parallel plate model of chips, and (c) shear strain triangle (Ref 28)



**Fig. 2** Collected Ti-15V-3Cr-3Al-3Sn chips

microstructures in the primary and secondary shear zones employing machining chips of Ti-15V-3Cr-3Al-3Sn produced with conventional turning and UAT.

## 2. Materials and Methods

Machining chips were obtained with conventional and UAT; both machining operations were performed without coolant or lubricant to avoid contamination. The turning was carried out with a cutting speed of 10 m/min, a feed rate of 0.1 mm/rev with a cutting depth of 100  $\mu\text{m}$ . Turning was performed for 500 s for each experiment run. Machining tools were made of cemented carbide coated with titanium-aluminum-nitride layer and with a nose radius of 0.8 mm. The cutting tool was normal to the work-piece axis, and the effective rake angle was  $\sim 14^\circ$ . In order to circumvent the influence caused by the wear of machining tool, a new tool was used for each experimental run. For the UAT process, the vibration of the machining tool was monitored by a noncontacted Polytec laser vibrometer (Model: OFV-3001). The imposed vibration was imposed in a tangential direction and its frequency was  $\sim 20$  kHz. A detailed experimental setup of UAT was described elsewhere (Ref 9, 10).

Continuous chips were collected in form of a curl, as shown in Fig. 2. To avoid substantial microstructural difference of the examined chip, the chip near the beginning or the end of the test was not used in this study. In order to reveal the cross-sectional microstructure, the chips were mounted edge-on in conductive Bakelite, and a bulk metal sample was also prepared along the cross section. Samples were ground on progressively

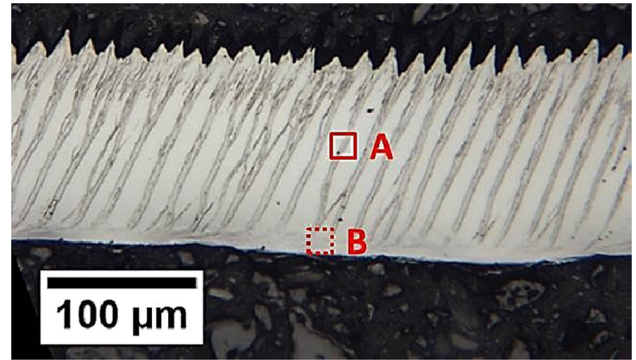


**Fig. 3** Optical micrograph of CT Ti-15V-3Cr-3Al-3Sn chip showing primary (a) and secondary (b) shear zones

finer silicon carbide papers, followed by polishing with 6 and 1  $\mu\text{m}$  diamond solutions, and finished with a final polish using a mixture of colloidal silica and hydrogen peroxide (20%) to remove stresses induced during mechanical grinding. The thickness of chips was measured on optical micrographs using ImageJ. For both machining processes, typically 20 measurements were performed to determine the average thickness of the chips. Electron backscatter diffraction (EBSD) was performed using a LEO 1530 VP field emission gun scanning electron microscope (FEG-SEM) equipped with a HKL Nordlys F high-speed EBSD camera. Site-specific transmission electron microscopy (TEM) specimens were lifted out by using an FEI Nova 600 Nanolab Dual-Beam focused ion beam (FIB) SEM, and the nonsite-specific TEM samples were prepared by mechanical polishing to 50  $\mu\text{m}$  followed by argon ion milling (gun current of 2.6 mA, voltage of 7 kV and angle of  $\pm 10^\circ$ ). The TEM analysis was conducted using JEOL 2000FX operated at 200 keV.

## 3. Results and Discussion

### 3.1 Ultrafine-Grained Microstructure in CT Machining Chips

A typical optical micrograph of a chip's cross section of conventionally turned Ti-15V-3Cr-3Al-3Sn is shown in Fig. 3. The primary and secondary shear zones appear darker compared with surrounding matrix (as indicated by squares A and B in Fig. 3).

A SEM image of the cross section of a CT Ti-15V-3Cr-3Al-3Sn (Fig. 4) shows finer microstructures in the primary and



secondary shear zones, marked by arrows A and B in Fig. 4, with clear boundaries between the shear zones and segment areas, similar to those reported elsewhere (Ref 30, 31). However, no detailed microstructural characterization was

reported in the literature to illustrate structural features in these shear zones.

To understand the evolution of shear zones further, both SEM-EBSD and TEM were performed. The former was carried out in a region containing shear bands from primary shear zones, as shown in Fig. 5. As indicated in an inverse pole figure (IPF) orientation map (Fig. 5b), the segments adjacent to the shear bands have the same orientation (same color), which implies that the segments are likely to belong to the same grain before the chip was separated from the bulk. An EBSD IPF orientation map (Fig. 6a) of another primary shear region exhibits shear bands formed continuously across two grains with misorientation of about  $30^\circ$  (Fig. 6b). This suggests that during the primary shear zone formation, catastrophic shear failure occurred at a very narrow shear zone leaving the adjacent matrix largely undeformed. In this study, the depth of cut ( $t_0$ ) is  $100\ \mu\text{m}$ , and the measured chip thickness ( $t_c$ ) is approximately  $135 \pm 4\ \mu\text{m}$ . Thus, according to Eq 1 and 2, the shear angle ( $\phi$ ) is  $\sim 41.2^\circ$  and the imposed shear strain is approximately 1.67. Significant grain refinement was reported for ECAP-processed pure Ti with imposed shear strain of 0.6 (Ref 32). Therefore, with the shear strain of 1.67, large grain refinement is expected in Ti-15V-3Cr-3Al-3Sn.

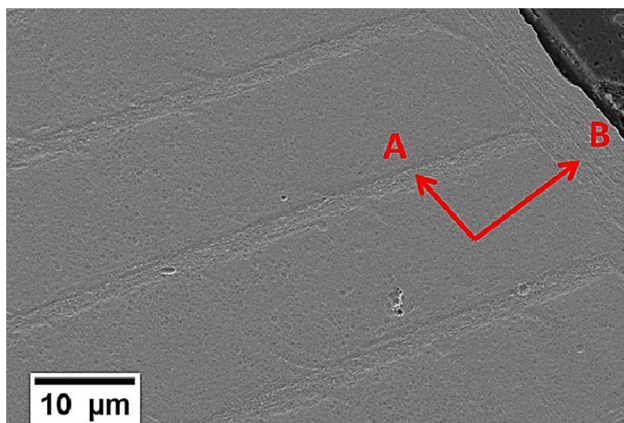


**Fig. 4** SEM micrograph of CT Ti-15V-3Cr-3Al-3Sn chip cross section: (A) primary shear zone; (B) secondary shear zones

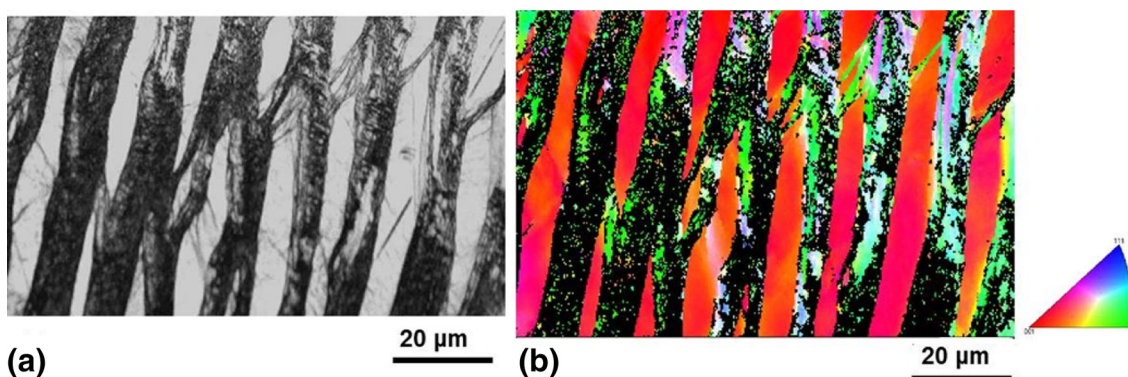


**Fig. 5** Band contrast image (a) and IPF orientation map (b) of CT-produced Ti-15V-3Cr-3Al-3Sn chip (The inset is the color scheme of the corresponding orientation map.)

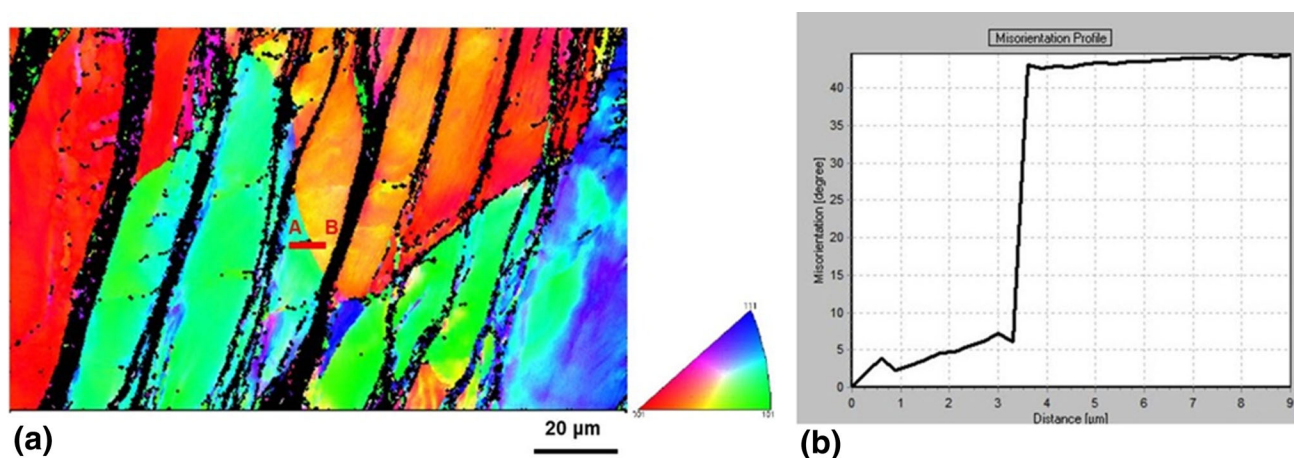


**Fig. 6** (a) SEM-EBSD IPF orientation map of CT-produced Ti-15V-3Cr-3Al-3Sn chip. (The inset is the color scheme of the corresponding orientation map.) (b) Misorientation profile from point A to B in (a)

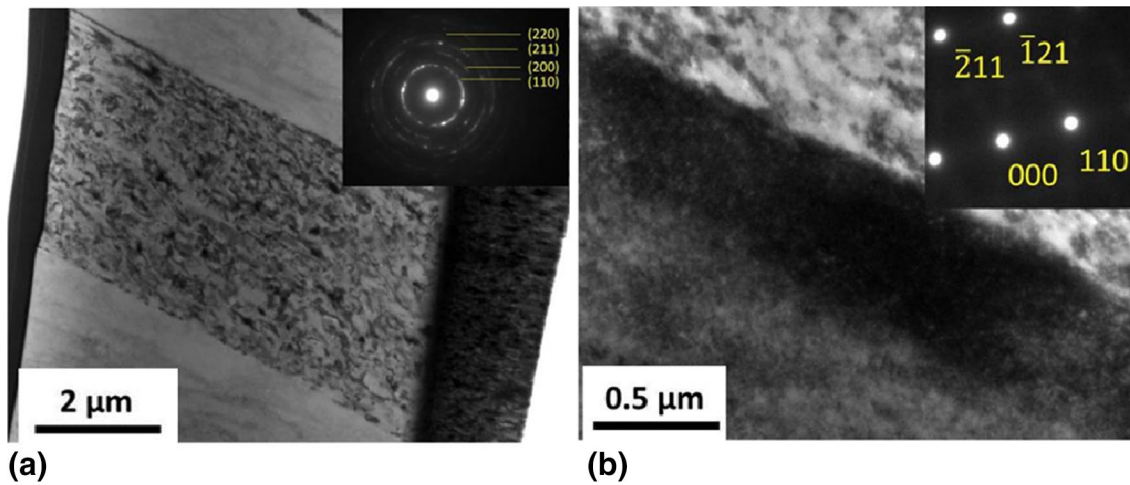


**Fig. 7** TEM micrographs of CT-produced Ti-15V-3Cr-3Al-3Sn chip at cross section of primary shear zone (a) with inset showing SAD pattern taking from nanocrystalline region and interface between nanocrystalline zone and adjacent matrix (b) (The inset in (b) is the diffraction pattern of the matrix; the beam direction is  $[1\bar{1}3]$ .)

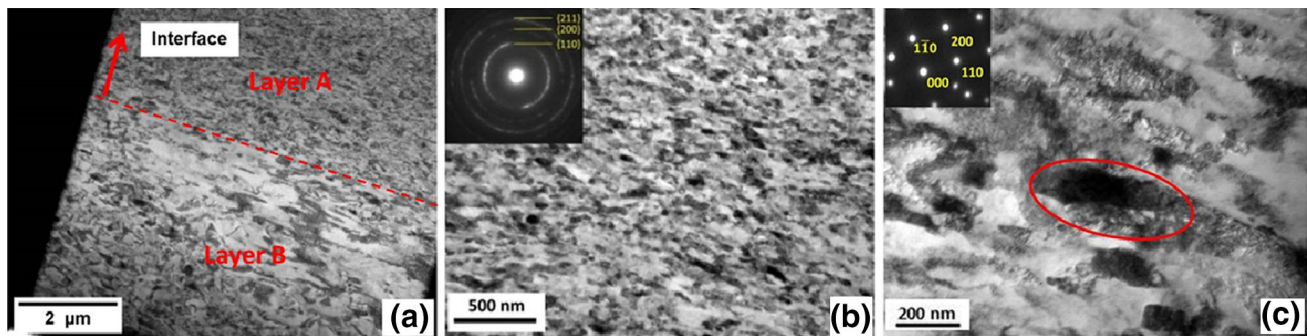


**Fig. 8** TEM micrographs of CT-produced Ti-15V-3Cr-3Al-3Sn chip in cross section of secondary shear zone: (a) low magnification, (b) nano-sized grains near interface (layer A), (c) elongated grains away from the interface (layer B)

In this study, severe plastic deformation at the primary shear zones impeded the quality of diffraction patterns. As a result, no information on grain morphology and orientation could be obtained with EBSD. Therefore, a site-specific TEM sample, containing one primary shear band and the surrounding matrix as indicated by square A in Fig. 3, was lifted out to reveal the microstructure of shear bands.

Figure 7a shows a TEM micrograph of the primary shear zone in CT-produced Ti-15V-3Cr-3Al-3Sn chips. A ring-shape corresponding selected area diffraction (SAD) pattern confirms that the  $\beta$  phase in the central band is nanocrystalline. The average grain size of this nanocrystalline region is  $\sim 80$  nm. The mechanism for generation of nanocrystalline grains in the primary shear zone involves formation of dislocation cell structures. Usually, the dislocation cells form in the early stages of plastic deformation. With the accumulation of misorientation between neighboring dislocation cells, the cells transform into the final fine-grain structures (Ref 33). Estrin et al. (Ref 34) developed a constitutive model, which applies to the dislocation cells, addressing sufficiently large strains. The model assumes that the average dislocation cell size,  $d$ , is inversely proportional to the square root of dislocation density,  $\rho$ :

$$d = \frac{K}{\sqrt{\rho}}, \quad (\text{Eq 3})$$

where  $K$  is a constant. It is known that during the machining process, a large amount of dislocations are generated because of the imposed high shear strain in the primary shear zone and hence the formation of nanocrystalline grains.

There is a sharp boundary between the nanocrystalline region and the adjacent matrix, which is consistent with our observations with SEM; this interface at higher magnification is shown in Fig. 7(b). A SAD pattern taken from the adjacent matrix comprises a regular spot pattern indicating a large grain size. No grain refinement or dislocations were found in the adjacent matrix. This finding proves that the high level of shear strains are only localized at the narrow primary shear zone and have a negligible effect on the surrounding matrix. The sharpness of the shear deformation region was also observed in face-centered cubic metals, e.g., copper, with quick-stop optical microscopy during machining (Ref 35).

The microstructure of a secondary shear zone was observed in a TEM sample lifted out from the area indicated by square B in Fig. 3. In contrast to the primary shear zone, the secondary



shear zone consists of two distinct layers: layer A near the tool tip-chip interface and layer B further away from the tool tip (Fig. 8a). At higher magnification, a nanocrystalline

microstructure of layer A is shown in Fig. 8(b); the corresponding SAD has a ring pattern. The average grain size in this region is approx. 80 nm. Below the nanocrystalline area (layer A), layer B contained elongated grains (marked with a circle in Fig. 8c). Compared to Fig. 8(b), the grains in Fig. 8(c) appear larger, with an average grain size of  $\sim 150$  nm.

A comparison with the primary shear zone (Fig. 7) demonstrates that the nanostructure region in the secondary shear zone (Fig. 8) is relatively wider with heterogeneous grain size distribution. This phenomenon can be explained with the aid of finite-element modeling of similar microstructures formed in carbon steel chips (Ref 36). The study suggested that the effective strain gradually attenuated with an increasing distance from the tool tip-chip interface, since the material near that interface might be subjected to friction-induced deformation followed by shearing in the primary shear zone (Ref 36). Therefore, the grain refinement effect is more significant near the chip surface, and bigger and elongated grains were observed away from the chip surface.

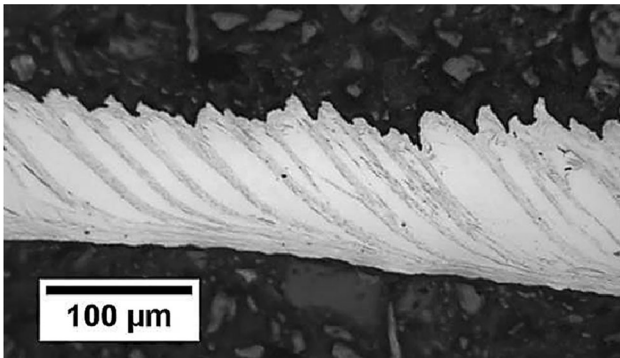


**Fig. 9** Optical micrograph of cross section of UAT-produced Ti-15V-3Cr-3Al-3Sn chip

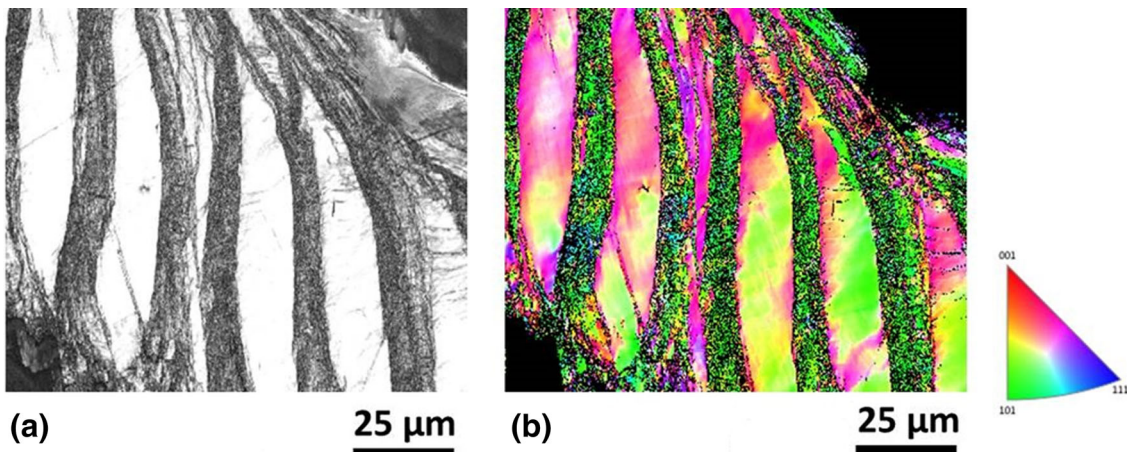


**Fig. 10** Band contrast image (a) and IPF orientation map (b) of UAT-produced Ti-15V-3Cr-3Al-3Sn machining chip (the inset is the color scheme of the corresponding orientation map)

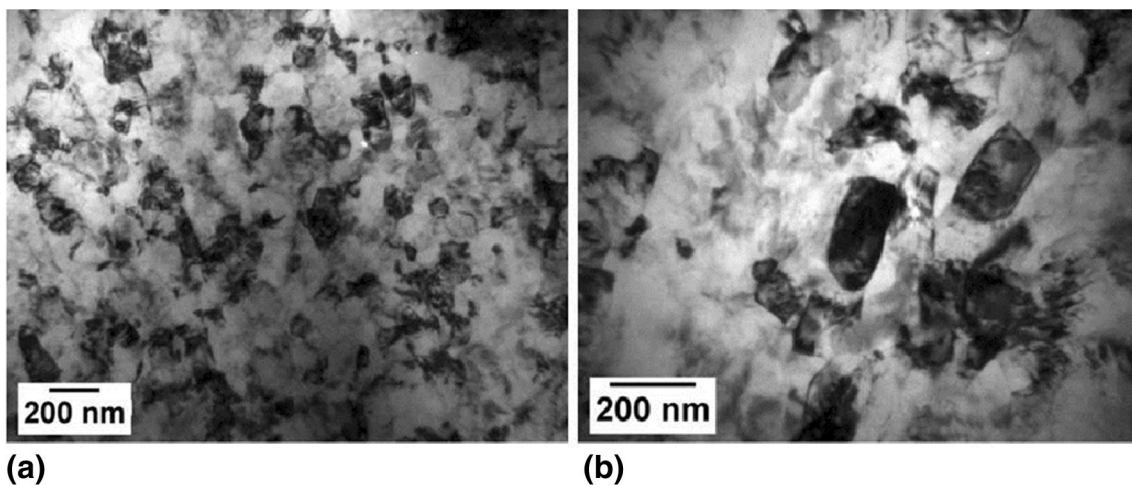


**Fig. 11** TEM micrographs of the primary shear zone in UAT-produced Ti-15V-3Cr-3Al-3Sn chip (a) nanostructure region and (b) individual large grains

### 3.2 Microstructure of UAT Ti-15V-3Cr-3Al-3Sn Chips

An optical micrograph of Ti-15V-3Cr-3Al-3Sn chip obtained with UAT (Fig. 9) demonstrates that its cross-sectional microstructure is similar to that of CT chips. Clear boundaries could also be observed between the shear zones and the surrounding matrix. It is noted that the thickness of the UAT chip is  $\sim 110 \pm 8 \mu\text{m}$ , less than that of the CT chip ( $\sim 135 \pm 4 \mu\text{m}$ ). Using Eq 2, the calculated shear plane angle is  $\sim 49.2^\circ$ . It is known that a larger shear plane angle results in a smaller shear plane area and hence a lower chip-formation shear force, which facilitates the machining process (Ref 28). This result mutually corroborates with the previous studies

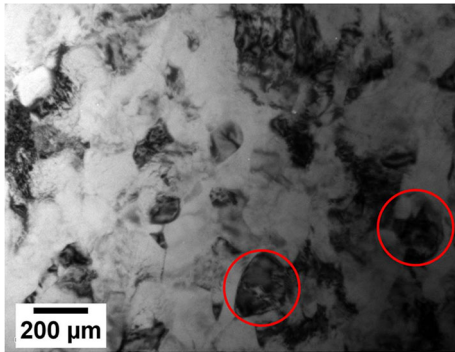


**Fig. 12** TEM micrograph of the secondary shear zone in UAT-produced chip

carried out with Ti-15V-3Cr-3Al-3Sn (Ref 9-11), according to which the measured cutting forces during UAT were observed to reduce in excess of 70% compared with CT. In addition to reduced cutting force, the improved surface quality also benefits from the lower friction in UAT (Ref 10).

Compared with CT, the increase of the shear plane angle for UAT is attributed to the reduction of friction between the machining tool and the chips (Ref 37). The reduced friction during UAT process can be explained based on the fact that due to a high-frequency vibration subjected to the tool, the elastic-plastic behavior of the titanium alloy is changed, i.e., quasiviscous friction occurs in the tool tip-chip interface (Ref 10, 38). Because of the acoustic softening effect, the critical static shear stress for plastic deformation is reduced under ultrasonic excitation (Ref 39). In addition, another cause of the reduced friction may be due to the increase in temperature in UAT chip during processing (Ref 40): the yield strength of the material at the tool tip-chip interface decreased due to the hot softening effect.

A SEM-EBSD orientation map showing the cross-sectional microstructure of the UAT chip is presented in Fig. 10. According to Eq 1, the shear strain in the primary shear zone is  $\sim 1.57$ , lower than that in the CT machining chips but still high enough to refine the grains in the narrow region. The TEM micrograph (Fig. 11a) confirms the formation of ultrafine grains in the primary shear zone for the UAT chips. Compared with CT, the most distinguishable difference in the primary shear zone is the larger grain size in UAT chip: the average grain size is  $\sim 110 \text{ nm}$ . In addition, the ultrafine-grain region in the UAT

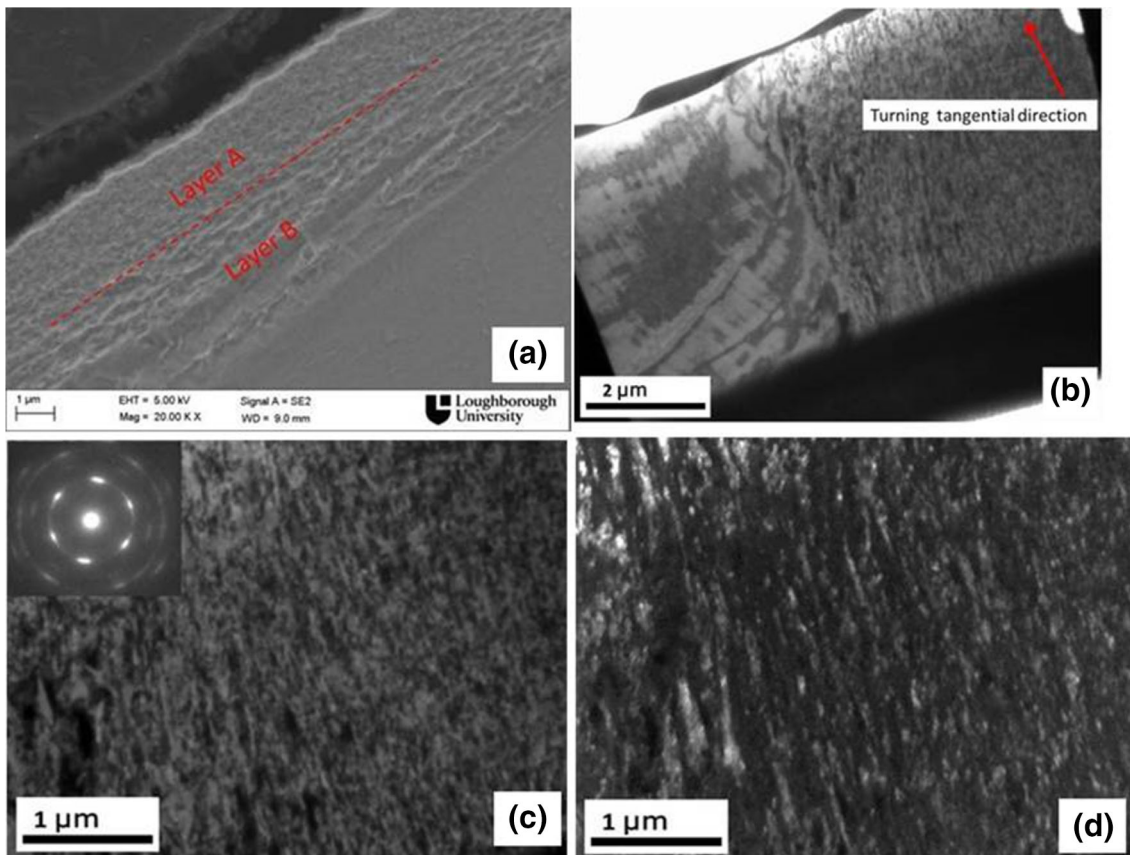


**Fig. 13** Deformed layer of CT-produced Ti-15V-3Cr-3Al-3Sn work-piece surface: (a) SEM, (b) TEM, (c) bright-field image of nanocrystalline grains, (d) corresponding dark-field image showing grains with one set of  $\langle 110 \rangle$  parallel to turning tangential direction



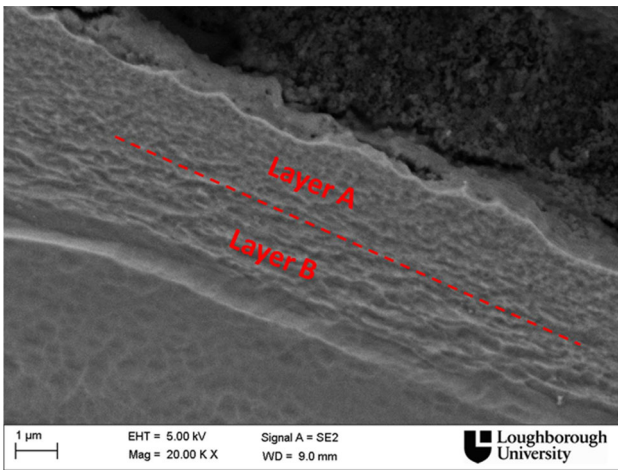


**Fig. 14** Severely deformed layer of UAT-produced Ti-15V-3Cr-3Al-3Sn work-piece subsurface

chip was less homogeneous than the CT one: some grains of size  $\sim 180$  nm were found, as shown in Fig. 11(b).

A comparison between the optical micrographs of CT and UAT chips (Fig. 3, 9) indicates that the thicknesses of the secondary shear zones for the CT and UAT chips are similar: both of them are  $\sim 10$   $\mu\text{m}$ . Figure 12 shows the TEM micrograph of the secondary shear zone in the chip produced by UAT. It reveals that ultrafine grains also formed during UAT process, however, due to the lower frictional force, the grain size is larger than that in the CT chips, moreover some grains of size  $\sim 200$  nm were observed, as indicated by circles.

### 3.3 Microstructure of Work-Piece Subsurface

It is known that a secondary shear zone is a surface, where chips are stripped off from a work-piece. Therefore, a subsurface microstructure of the work-piece is supposed to be identical to that of the secondary shear zone (Ref 41).

A SEM micrograph of the CT work-piece surface (Fig. 13a) exhibits a deformation layer of  $\sim 5$   $\mu\text{m}$  on the subsurface. Here two layers with different grain sizes can be identified marked as layers A and B in Fig. 13(a). This result is consistent with observations in the TEM micrograph of the CT-produced chip (Fig. 8a). Figure 13(b) confirms that the deformation layer has a nanocrystalline microstructure and a clear boundary separating a heavily deformed region from that with the original microstructure. At higher magnification, it is obvious that the grains are elongated along the turning tangential direction in the nanocrystalline region (Fig. 13c). A ring-shape SAD pattern with six strong spots implies that the grains in this nanocrystalline zone have preferred orientation in  $\langle 110 \rangle$  direction parallel to the turning tangential direction.

The cross-sectional microstructure of the UAT work-piece subsurface is presented in Fig. 14. A similar severely deformed layer of  $\sim 5$   $\mu\text{m}$  in thickness was produced during UAT, within which two layers with different grain sizes can be observed.

## 4. Conclusions

In this study, the microstructures of Ti-15V-3Cr-3Al-3Sn chips produced with conventional and UAT techniques were investigated. The major conclusions are as follows:

- The primary shear zone in CT chips consists of a homogeneous nanomicrostructure with clear boundaries with the surrounding undeformed matrix.
- The ultrafine-grain region in the secondary shear zone for CT process is less homogeneous than that in the primary shear zone due to the effective strain attenuation.
- As a result of reduced frictional force, machining chips produced by UAT demonstrate a larger shear plane angle and lower shear strain. Larger grains were observed in the primary and secondary shear zones.
- A heavily deformed layer with depth of about 5  $\mu\text{m}$  was formed at the surface of the machined bulk material replicating the microstructure of the secondary shear zone of the machining chips. Its nanocrystalline grains were equiaxed close to the surface and were elongated along the turning tangential direction  $\sim 1$  or 2  $\mu\text{m}$  away from it.

## References

1. R.R. Boyer and R.D. Briggs, The Use of  $\beta$  Titanium Alloys in the Aerospace Industry, *J. Mater. Eng. Perform.*, 2005, **14**, p 681–685
2. J. Sun and Y.B. Guo, A Comprehensive Experimental Study on Surface Integrity by End Milling Ti-6Al-4V, *J. Mater. Process. Technol.*, 2009, **209**, p 4036–4042
3. C. Brecher, C.J. Rosen, and M. Emonts, Laser-Assisted Milling of Advanced Materials, *Phys. Proc.*, 2010, **5**, p 259–272
4. R. Muhammad, A. Naseer, A. Roy, and V.V. Silberschmidt, Numerical Modelling of Vibration-Assisted Turning of Ti-15333, *Proc. CIRP*, 2012, **1**, p 347–352
5. A. Maurotto, R. Muhammad, A. Roy, V.I. Babitsky, and V.V. Silberschmidt, Comparing Machinability of Ti-15-3-3-3 and Ni-625 Alloys in Uat, *Proc. CIRP*, 2012, **1**, p 330–335
6. R. Muhammad, N. Ahmed, A. Roy, and V.V. Silberschmidt, Turning of Advanced Alloys with Vibrating Cutting Tool, *Solid State Phenom.*, 2012, **188**, p 277–284
7. R. Muhammad, M. Demiral, A. Roy, and V.V. Silberschmidt, Modelling the Dynamic Behaviour of Hard-to-Cut Alloys Under Conditions of Vibro-Impact Cutting, *J. Phys. Conf. Ser.*, 2013, **451**(1), p 012030
8. R. Muhammad, A. Roy, and V. V. Silberschmidt, Finite Element Modelling of Conventional and Hybrid Oblique Turning Processes of Titanium Alloy, *14th CIRP Conference on Modelling of Machining Operations*, 2013, p 510–515
9. R. Muhammad, A. Maurotto, M. Demiral, A. Roy, and V.V. Silberschmidt, Thermally Enhanced Ultrasonically Assisted Machining of Ti Alloy, *CIRP J. Manuf. Sci. Technol.*, 2014, **7**, p 159–167
10. A. Maurotto, R. Muhammad, A. Roy, and V.V. Silberschmidt, Enhanced Ultrasonically Assisted Turning of a  $\beta$ -Titanium Alloy, *Ultrasonics*, 2013, **53**, p 1242–1250
11. R. Muhammad, A. Maurotto, A. Roy, and V.V. Silberschmidt, Hot Ultrasonically Assisted Turning of  $\beta$ -Ti Alloy, *Proc. CIRP*, 2012, **1**, p 336–341
12. V.I. Babitsky, A.V. Mitrofanov, and V.V. Silberschmidt, Ultrasonically Assisted Turning of Aviation Materials: Simulations and Experimental Study, *Ultrasonics*, 2004, **42**(1–9), p 81–86
13. N. Ahmed, A.V. Mitrofanov, V.I. Babitsky, and V.V. Silberschmidt, Analysis of Forces in Ultrasonically Assisted Turning, *J. Sound Vib.*, 2007, **308**(3–5), p 845–854
14. P.-J. Arrazola, A. Garay, L.-M. Iriarte, M. Armendia, and S. Marya, Machinability of Titanium Alloys (Ti6Al4V) and Ti555.3, *J. Mater. Process. Technol.*, 2009, **209**, p 2223–2230
15. A.I.S. Antonialli, A.A.M. de Filho, V.L. Sordi, and M. Ferrante, The Machinability of Ultrafine-Grained Grade 2 Ti Processed by Equal Channel Angular Pressing, *J. Mater. Res. Technol.*, 2012, **1**, p 148–153
16. C. Ohkubo, I. Watanabe, J.P. Ford, H. Nakajima, and T. Tosoi, The Machinability of Cast Titanium and Ti-6Al-4V Alloy, *Int. J. Mach. Tool Manuf.*, 2001, **41**, p 1055–1070

17. J. Barry, G. Byrne, and D. Lennon, Observation of Chip Formation and Acoustic Emission in Machining Ti-6Al-4V Alloy, *Int. J. Mach. Tool Manuf.*, 2001, **41**, p 1055–1070
18. G. Sutter and G. List, Very High Speed Cutting of Ti-6Al-4V Titanium Alloy—Change in Morphology and Mechanism of Chip Formation, *Int. J. Mach. Tool Manuf.*, 2013, **66**, p 37–43
19. J. Hua and R. Shivpuri, Prediction of Chip Morphology and Segmentation During the Machining of Titanium Alloys, *J. Mater. Process. Technol.*, 2004, **150**, p 124–133
20. M.J. Bermingham, S. Palanisamy, D. Kent, and M.S. Dargusch, A Comparison of Cryogenic and High Pressure Emulsion Cooling Technologies on Tool Life and Chip Morphology in Ti-6Al-4V Cutting, *J. Mater. Process. Technol.*, 2012, **212**, p 752–765
21. S. Cedergren, G. Petti, and G. Sjöberg, On the Influence of Work Material Microstructure on Chip Formation, Cutting Forces and Acoustic Emission When Machining Ti-6Al-4V, *Proc. CIRP*, 2013, **12**, p 55–60
22. S. Sun, M. Brandt, and M.S. Dargusch, Characteristics of Cutting Forces and Chip Formation in Machining of Titanium Alloys, *Int. J. Mach. Tool Manuf.*, 2009, **49**, p 561–568
23. M. Sima and T. Özel, Modified Material Constitutive Models for Serrated Chip Formation Simulations and Experimental Validation in Machining of Titanium Alloy Ti-6Al-4V, *Int. J. Mach. Tool Manuf.*, 2010, **50**, p 943–960
24. M. Calamaz, D. Coupard, and F. Girot, A New Material Model for 2D Numerical Simulation of Serrated Chip Formation When Machining Titanium Alloy Ti-6Al-4V, *Int. J. Mach. Tool Manuf.*, 2008, **48**, p 275–288
25. A. Molinari, C. Musquar, and G. Sutter, Adiabatic Shear Banding in High Speed Machining of Ti-6Al-4V: Experiments and Modelling, *Int. J. Plast.*, 2002, **18**, p 443–459
26. R. Shivpuri, J. Hua, P. Mittal, A.K. Srivastava, and G.D. Lahoti, Microstructure-Mechanics Interactions in Modelling Chip Segmentation During Titanium Machining, *CIRP Ann. Manuf. Technol.*, 2002, **51**, p 71–74
27. Y. Karpat, Temperature Dependent Flow Softening of Titanium Alloy Ti6Al4V: An Investigation Using Finite Element Simulation of Machining, *J. Mater. Process. Technol.*, 2011, **211**, p 737–749
28. M.P. Groover, *Fundamentals of Modern Manufacturing Materials, Processes, and Systems*, 3rd ed., Wiley, New York, 2007
29. M.C. Shaw, *Metal Cutting Principle*, 2nd ed., Oxford University Press, Oxford, 2005
30. P. Rokicki, K. Nowag, Z. Spetz, L. Fusova, K. Saksli, R. Ghisleni, and C. Siemers, Microstructural Characteristic of Ti-15V-3Al-3Sn-3Cr Chips, *Int. J. Earth Sci.*, 2010, **55**, p 452–456
31. P. Rokicki, K. Nowag, Z. Spetz, L. Fusova, K. Saksli, R. Ghisleni, C. Siemers, Chip Formation Process of Ti-15V-3Al-3Sn-3Cr Alloy, *19th International Conference on Metallurgy and Materials*, vol. METAL, 2010, p 844–849
32. X. Zhao, W. Fu, X. Yang, and T.G. Langdon, Microstructure and Properties of Pure Titanium Processed by Equal-Channel Angular Pressing at Room Temperature, *Scr. Mater.*, 2008, **59**, p 542–545
33. U.F. Kocks and H. Mecking, Physics and Phenomenology of Strain Hardening: The FCC Case, *Prog. Mater. Sci.*, 2003, **48**(3), p 171–273
34. Y. Estrin, L.S. Tóth, A. Molinari, and Y. Bréchet, A Dislocation-Based Model for All Hardening Stages in Large Strain Deformation, *Acta Mater.*, 1998, **46**(15), p 5509–5522
35. S. Swaminathan, M. Ravi Shankar, S. Lee, J. Hwang, A.H. King, R.F. Kezar, B.C. Rao, T.L. Brown, S. Chandrasekar, W.D. Compton, and K.P. Trumble, Large Strain Deformation and Ultrafine Grained Materials by Machining, *Mat. Sci. Eng. A*, 2005, **410–411**, p 358–363
36. W.J. Deng, W. Xia, C. Li, and Y. Tang, Ultrafine Grained Material Produced by Machining, *Mater. Manuf. Process.*, 2010, **25**, p 355–359
37. S.Y. Hong, Y. Ding, and W. Jeong, Friction and Cutting Forces in Cryogenic Machining of Ti-6Al-4V, *Int. J. Mach. Tool Manuf.*, 2001, **41**(15), p 2271–2285
38. V.K. Astashev and V.I. Babitsky, Ultrasonic Cutting as a Nonlinear (Vibro-Impact) Process, *Ultrasonics*, 1998, **36**, p 89–96
39. B. Langenecker, Effects of Ultrasound on Deformation Characteristics of Metals, *IEEE Trans. Sonic Ultrason.*, 1966, **13**, p 12–13
40. R. Muhammad, M.S. Hussain, A. Maurotto, C. Siemers, A. Roy, and V.V. Silberschmidt, Analysis of a Free Machining  $\alpha + \beta$  Titanium Alloy Using Conventional and Ultrasonically Assisted Turning, *J. Mater. Process. Technol.*, 2014, **214**(4), p 906–915
41. S. To, Y.H. Zhu, and W.B. Lee, Effects of Cutting Depth on the Surface Microstructure of a Zn-Al Alloy During Ultra-Precision Machining, *Appl. Surf. Sci.*, 2008, **254**(6), p 1559–1564